

See discussions, stats, and author profiles for this publication at: <https://www.researchgate.net/publication/269871723>

The Electronic Structure of $\text{CH}_3\text{NH}_3\text{PbX}_3$ Perovskites; the Dependence on the Halide Moiety

ARTICLE in THE JOURNAL OF PHYSICAL CHEMISTRY C · DECEMBER 2014

Impact Factor: 4.77 · DOI: 10.1021/jp509460h

CITATIONS

10

READS

264

14 AUTHORS, INCLUDING:



D. D. Sarma

Indian Institute of Science

485 PUBLICATIONS 11,684 CITATIONS

SEE PROFILE



Olof Karis

Uppsala University

115 PUBLICATIONS 2,712 CITATIONS

SEE PROFILE

Electronic Structure of $\text{CH}_3\text{NH}_3\text{PbX}_3$ Perovskites: Dependence on the Halide Moiety

Rebecka Lindblad,^{*,†} Naresh K. Jena,[‡] Bertrand Philippe,[†] Johan Oscarsson,[†] Dongqin Bi,[§] Andreas Lindblad,^{||} Suman Mandal,[⊥] Banabir Pal,[⊥] D. D. Sarma,[⊥] Olof Karis,[†] Hans Siegbahn,[†] Erik M. J. Johansson,[§] Michael Odelius,[‡] and Håkan Rensmo^{*,†}

[†]Department of Physics and Astronomy, Molecular and Condensed Matter Physics, Uppsala University, Box 516, 751 20 Uppsala, Sweden

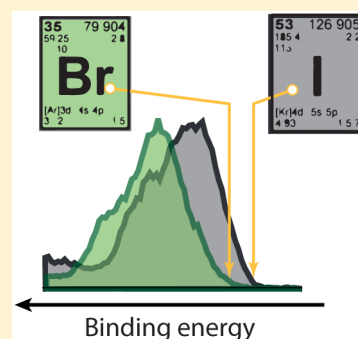
[‡]Department of Physics, AlbaNova University Center, Stockholm University, 106 91 Stockholm, Sweden

[§]Department of Chemistry, Ångström, Uppsala University, Box 523, 751 20 Uppsala, Sweden

^{||}Department of Chemistry, Ångström, Inorganic Chemistry, Uppsala University, Box 538, 751 21 Uppsala, Sweden

[⊥]Solid State and Structural Chemistry Unit, Indian Institute of Science, Bangalore 560012, India

ABSTRACT: A combination of measurements using photoelectron spectroscopy and calculations using density functional theory (DFT) was applied to compare the detailed electronic structure of the organolead halide perovskites $\text{CH}_3\text{NH}_3\text{PbI}_3$ and $\text{CH}_3\text{NH}_3\text{PbBr}_3$. These perovskite materials are used to absorb light in mesoscopic and planar heterojunction solar cells. The Pb 4f core level is investigated to get insight into the chemistry of the two materials. Valence level measurements are also included showing a shift of the valence band edges where there is a higher binding energy of the edge for the $\text{CH}_3\text{NH}_3\text{PbBr}_3$ perovskite. These changes are supported by the theoretical calculations which indicate that the differences in electronic structure are mainly caused by the nature of the halide ion rather than structural differences. The combination of photoelectron spectroscopy measurements and electronic structure calculations is essential to disentangle how the valence band edge in organolead halide perovskites is governed by the intrinsic difference in energy levels of the halide ions from the influence of chemical bonding.



INTRODUCTION

The recent advancement of perovskites as photovoltaic material has given a new dimension to the conventional solar cell research paradigm. Organolead halide perovskites, in particular, have recently drawn much attention as light absorbers in mesoscopic solar cells.^{1–3} In mesoscopic devices, the perovskite is incorporated into a mesoporous network of a large bandgap semiconductor or insulator.^{4–7} Because of the favorable light absorbing properties together with high electron and hole conduction, the perovskite material also works as a thin film absorber in layered structures.^{8–11}

The general chemical formula of methylammonium halide perovskites is $\text{CH}_3\text{NH}_3\text{PbX}_3$, where X can be different combinations of I, Br, and Cl. In this study we focus on perovskites including the halide I and Br as in $\text{CH}_3\text{NH}_3\text{PbI}_3$ and $\text{CH}_3\text{NH}_3\text{PbBr}_3$. Because of its smaller bandgap, $\text{CH}_3\text{NH}_3\text{PbI}_3$ gives a broader light absorption in the visible region compared to $\text{CH}_3\text{NH}_3\text{PbBr}_3$. $\text{CH}_3\text{NH}_3\text{PbBr}_3$ has, on the other hand, shown the potential to give solar cells with a higher open circuit voltage (V_{oc}),¹² and nanoparticles of this material show high stability.¹³

The function of the solar cells is to a large extent dependent on the energy level alignment between the different materials in the device and also on their electronic properties. Photoelectron spectroscopy is a method to directly probe the

occupied electronic levels in a material, and the experimental results are naturally related to calculations of the electronic structure allowing for a decomposition into element-specific contributions.^{8,14} In the literature, there are several investigations in which density functional theory (DFT) has been used to calculate the electronic band structure of various perovskites.^{15–17} In this study, we exploit the combination of photoelectron spectroscopy measurements using high excitation energies (hard X-ray photoelectron spectroscopy, HAXPES) and density functional calculations as a source of information to gain a detailed understanding of the electronic structure of organolead halide perovskites. A recent experimental study of the outermost energy levels in perovskite materials on TiO_2 using UV photoelectron spectroscopy (UPS) reveals a valence band edge of $\text{CH}_3\text{NH}_3\text{PbBr}_3$ at a higher binding energy compared to $\text{CH}_3\text{NH}_3\text{PbI}_3$.¹⁸ In the present study, we use a complementary experimental approach using HAXPES to investigate the electronic structure of these two materials and explain the observed differences using DFT calculations.

Received: September 18, 2014

Revised: December 17, 2014

Published: December 18, 2014



Compared to UPS, HAXPES allows for comparing core level and valence level results from the same surface with similar surface sensitivity. This can be utilized to characterize the chemistry in terms of, for example, oxidation state and stoichiometry and at the same time determine relative valence edge position and obtain an insight into the molecular orbital composition or the density of states structure. Moreover, HAXPES offers more bulk sensitive measurements compared to both UPS and traditional Al $K\alpha$ based XPS and can potentially be used to differentiate the bulk electronic structures from electronic effects due to specific surface structure and surface contamination. Because of a variation in photoionization cross section for each element, higher photon energies can also give enhanced weight to heavier elements. This can be made into an advantage when studying lead halide perovskites, and especially the valence levels since their electronic properties are believed to be largely determined by the lead halide framework.¹⁴ The electronic structure calculations provides a supplement to the experimental findings in terms of explaining the valence level spectra and also some key features in the core-level spectra.

■ EXPERIMENTAL SECTION

The experimentally studied samples consisted of thin films of $\text{CH}_3\text{NH}_3\text{PbI}_3$ and $\text{CH}_3\text{NH}_3\text{PbBr}_3$ perovskites deposited on fluorine-doped tin oxide (FTO). The $\text{CH}_3\text{NH}_3\text{PbI}_3$ perovskite was made by mixing equal moles of PbI_2 and $\text{CH}_3\text{NH}_3\text{I}$ in γ -butyrolactone as earlier reported.¹⁹ A similar procedure was used for $\text{CH}_3\text{NH}_3\text{PbBr}_3$ where dimethylformamide was used as solvent. The mixtures were then spin-coated onto FTO, and the coated films were heated to 100 °C for 20 min, during which the remaining solvent vaporizes. The samples were stored in an Ar-filled container directly after its preparation in order to reduce effects from moisture. The container was opened just before the photoelectron spectroscopy measurement.

Photoelectron spectroscopy measurements with hard X-rays (HAXPES) were performed at the high kinetic energy electron spectroscopy (HIKE) end station on beamline KMC-1 at Bessy II at Helmholtz-Zentrum in Berlin,²⁰ at a photon energy of 4000 eV, using the Si(311) crystal in the crystal monochromator. The experimental broadening (full width at half-maximum, fwhm) is below 0.3 eV. All spectra are binding energy calibrated using the metallic contribution to the Pb 4f_{7/2} core level. The binding energy of this level was measured for metallic lead and found to be 137.0 eV with respect to the Fermi level as measured on a Au sample. This value is in accordance with literature values.²¹

Some minor charging was observed in the measurements of both perovskite materials, possibly due to an insufficient contact between the FTO substrate and the perovskite film. The charging was controlled by following peak positions and peak shape with variations in light intensity. The same procedure was also used to check for X-ray-induced effects. While prolonged measurement shows such effects, no such effects were observed in the spectra reported here. A series of samples were measured, and the experimental spectra shown in this work are representative for all measured samples. The observed core level and valence level shifts were similar (within ± 0.1 eV) in all samples regardless of charging and method of binding energy calibration (via measurements of metallic lead or via measurements of a Sn core level from the FTO substrate).

■ COMPUTATIONAL DETAILS

The $\text{CH}_3\text{NH}_3\text{PbI}_3$ perovskite is modeled within periodic density functional theory (DFT) according to a recent report of the crystal structure²² where the tetragonal structure has lattice parameters $a = b = 8.85$ Å and $c = 12.64$ Å. For the perovskite $\text{CH}_3\text{NH}_3\text{PbBr}_3$, the lattice parameters are $a = b = 8.86$ Å and $c = 11.83$ Å.²³ In our calculation, we have employed a $2 \times 2 \times 2$ supercell, with approximate dimensions $17 \times 17 \times 25$ Å, containing 32 Pb^{2+} , 96 I^-/Br^- , and 32 CH_3NH_3^+ ions. The geometries of both the perovskite structures were optimized in the CPMD program²⁴ at experimental cell parameters.

The theoretical analysis of the electronic structure was derived from calculations in the CPMD program²⁴ and the CP2K package,²⁵ employing the BLYP functional augmented with van der Waals interactions.^{26–28} The calculations were performed at the Γ point. Against the background of earlier calculations,^{16,17} the neglect of k-point sampling is motivated by the size of the supercells.

In the CPMD program,²⁴ the Kohn–Sham orbitals and electron density were expanded in a plane wave basis set with kinetic energy cutoffs of 70/280 Ry, in combination with a pseudopotential description of the core levels. For carbon and nitrogen, we have used a Trouiller–Martins norm-conserving pseudopotential expressed in Kleinman–Bylander^{29,30} form and for hydrogen a local pseudopotential with a parametrized Gaussian. Godecker–Teter–Hutter (GTH) pseudopotentials have been employed for I, Br, and Pb (and for Bi in the $Z + 1$ approximation; see below).^{31,32}

In the CP2K package,²⁵ we have used the Gaussian and plane waves (GPW) method, based on GTH pseudopotentials, in the Quickstep (QS) code.^{33,34} The Kohn–Sham orbitals were described in local Gaussian DZVP^{31,35,36} basis set, and the electron density was expanded in a plane wave basis set with kinetic energy cutoff 70 Ry; basis set dependence up to 300 Ry was investigated.

To simulate the presence of metallic lead Pb^0 atoms, we have also created two defect perovskite structures from the $\text{CH}_3\text{NH}_3\text{PbI}_3$ structure by removing two I^- ions initially coordinated to a Pb^{2+} ion in an octahedral fashion. Two I^- ions in cis or trans position around a Pb^{2+} ion were removed to generate defect structures 1 and 2. For interpretation of the experimental X-ray photoelectron spectroscopy (HAXPES) data of the Pb core levels, we have, in the CPMD program,²⁴ computed the relative binding energies for all the Pb centers in the defect structures, within the $Z + 1$ approximation, by substituting a Pb atom by a Bi^+ ion.

The optimized structures for both the perovskites (pristine) are further considered for total density of state (DOS) and projected DOS (PDOS) calculations employing the CP2K package.²⁵ The calculated DOS and PDOS energies were convoluted by a Gaussian function with full width at half-maximum of 0.5 eV to obtain the spectra for direct comparison with the valence HAXPES spectra obtained experimentally. We have also estimated the effect of plane wave cutoff on the total DOS, and we note that there is no significant change of total DOS with increase of cutoff. Charge analysis were performed in the CP2K package on all structures. The charges given below are in units of e , the absolute value of the charge of the electron.

In the comparison of both orbital energies for valence-level and total energies in the $Z + 1$ approximation for core levels, the absolute energies from the two separate periodic

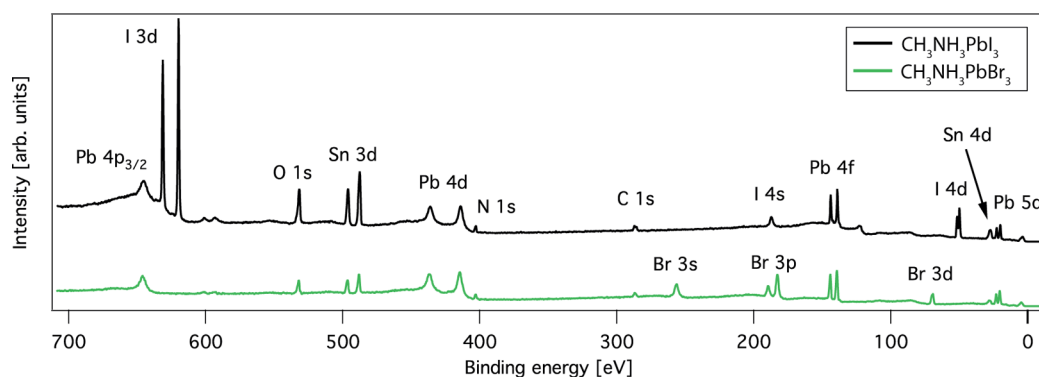


Figure 1. Overview spectra of samples with the two perovskites where also the FTO substrate can be seen. The intensities are scaled vs the Pb core levels.

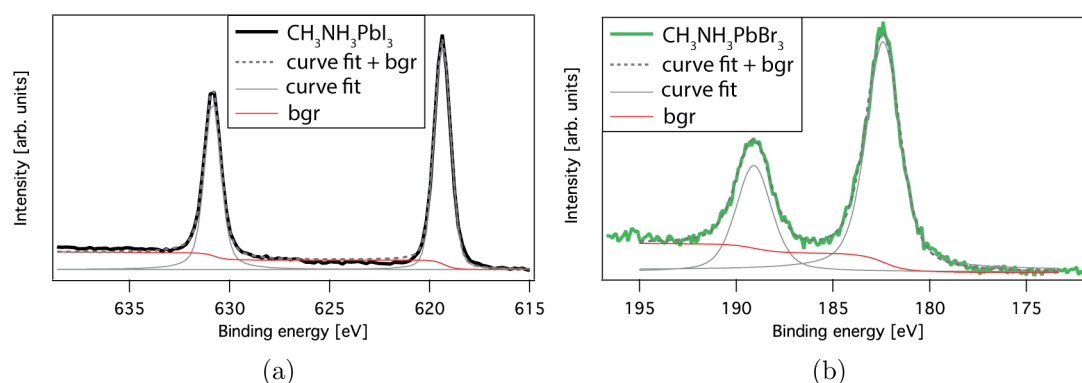


Figure 2. (a) I 3d core level in $\text{CH}_3\text{NH}_3\text{PbI}_3$ and (b) Br 3p core level in $\text{CH}_3\text{NH}_3\text{PbBr}_3$ peak fitted using Voigt functions and a Shirley background.

$\text{CH}_3\text{NH}_3\text{PbI}_3$ or $\text{CH}_3\text{NH}_3\text{PbBr}_3$ calculations are somewhat arbitrary, and we require a well-defined reference for our purpose to compare the valence band shift observed experimentally. In order to evaluate the relative energy scales of the $\text{CH}_3\text{NH}_3\text{PbI}_3$ or $\text{CH}_3\text{NH}_3\text{PbBr}_3$ calculations, we have generated a merged perovskite structure in which the two different perovskites are merged along the c -axis, and we reoptimized this structure with the cell parameters $a = b = 17.7020 \text{ \AA}$ and $c = 48.5480 \text{ \AA}$. We consider the merged system as the benchmark for the energy scale, and for the analysis of the valence levels we have applied energy shifts so that the C and N PDOS are in alignment with the experimental photoelectron spectra. From this alignment, we have deduced the energy shifts for the individual perovskite (I and Br) structures which are 3.7 and 2.9 eV, respectively, and these shifts are applied in the calculated valence level spectra shown in this work. The merged system was also used to simulate the Pb 4f core-level binding energy difference in $\text{CH}_3\text{NH}_3\text{PbI}_3$ and $\text{CH}_3\text{NH}_3\text{PbBr}_3$ by $Z + 1$ calculations for Pb atoms deep into the $\text{CH}_3\text{NH}_3\text{PbI}_3$ and $\text{CH}_3\text{NH}_3\text{PbBr}_3$ regions of the merged system.

RESULTS AND DISCUSSION

Core-Level Binding Energies. An overview of the photoelectron spectra of the $\text{CH}_3\text{NH}_3\text{PbI}_3$ and $\text{CH}_3\text{NH}_3\text{PbBr}_3$ samples are shown in Figure 1 containing all the expected core levels of the perovskites. It also contains small contributions from core levels in the FTO substrate. More detailed spectra of the I 3d, Br 3p, and Pb 4f core levels are shown in Figures 2 and 3, showing the quality of the samples.

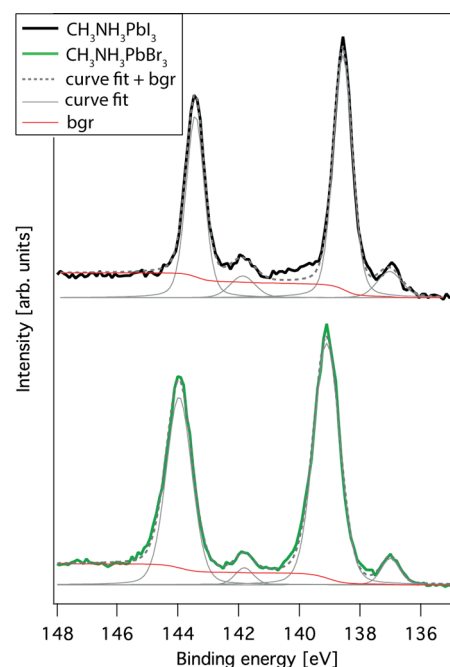


Figure 3. Measured Pb 4f core levels peak fitted using Voigt functions and a Shirley background.

The I 3d core level in Figure 2a shows narrow peaks (fwhm 1.0 eV) where the $\text{I } 3d_{5/2}$ level has a binding energy of 619.4 eV and a spin–orbit splitting to the $\text{I } 3d_{3/2}$ level of 11.5 eV, similar to what has been observed earlier.¹⁴ The Br 3p level is broader (fwhm 2.1 eV) compared to the I 3d level which can be

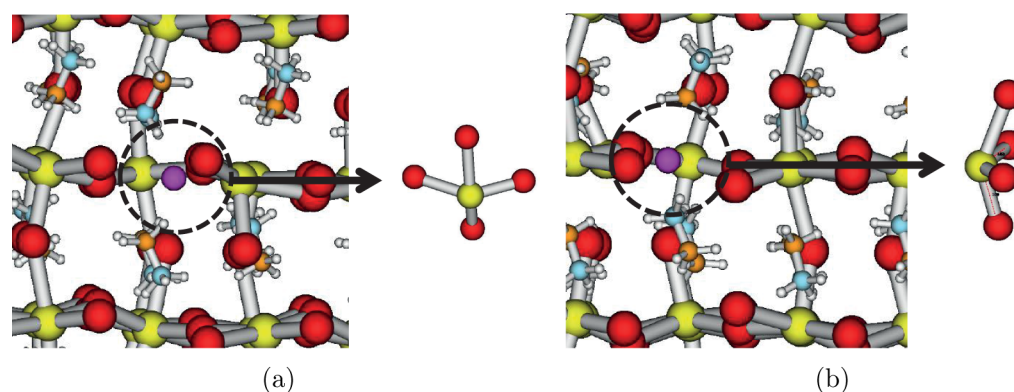


Figure 4. Undercoordinated Pb atom (purple, marked by the dotted ring) at the two defect structures, structure 1 (a) and structure 2 (b). A blown-up view of the defect site displays the local coordination.

explained by a larger lifetime broadening (2.15 eV for Br 3p compared to 0.56 eV for I 3d).³⁷ The Br 3p_{3/2} level has a binding energy of 182.4 eV and a splitting to the Br 3p_{1/2} level of 6.7 eV (see Figure 2b), as also found in other Pb_xBr_y compounds.^{38,39}

The experimental Pb 4f signal for the CH₃NH₃PbI₃ and CH₃NH₃PbBr₃ samples are shown in Figure 3. The spin–orbit splitting between the Pb 4f_{7/2} and 4f_{5/2} lines is 4.85 eV in both compounds. The CH₃NH₃PbI₃ sample shows a binding energy of 138.6 eV for the main Pb 4f_{7/2} contribution. However, in the spectra there is also a smaller contribution at a binding energy of 137.0 eV, thus representing a shift of 1.6 eV. The smaller contribution at lower binding energy that sometimes is visible in perovskites has earlier been assigned to metallic lead.^{8,14} The main contribution is assigned to Pb²⁺ in PbI₃.¹⁴ As a consequence of the calibration procedure of the photoelectron spectra, the feature from metallic lead remains at 137.0 eV also for the CH₃NH₃PbBr₃ sample. However, the Pb²⁺ lines are shifted to higher binding energies for CH₃NH₃PbBr₃ with Pb 4f_{7/2} at a binding energy of 139.1 eV, thus giving a shift of 0.5 eV compared to CH₃NH₃PbI₃. Accordingly, the metallic peak is for this material separated further away from the Pb²⁺ peak and the binding energy difference is 2.1 eV. The Pb 4f core-level peaks are also broader for the CH₃NH₃PbBr₃ sample with fwhm of 1.0 eV that can be compared to 0.75 eV for CH₃NH₃PbI₃, which could indicate a higher degree of charging in the CH₃NH₃PbBr₃ sample. A core level from the FTO substrate, Sn 4s, has a binding energy of approximately 141 eV and is therefore partly seen as an increased background at the high binding energy side of the Pb 4f_{7/2} peak (the Sn 4s core level is not included in the fitting of the Pb 4f core levels).

The relative binding energy of the Pb 4f core levels in the two perovskites was simulated using the $Z + 1$ approximation for the merged crystal, where a theoretical binding energy shift of 0.46 eV was found, i.e., very close to the experimental value of 0.5 eV. The shift of the Pb 4f levels can also be rationalized based on a charge analysis. For the CH₃NH₃PbI₃ perovskite, the charges on the Pb atoms are 0.13–0.14 *e* whereas in the bromine counterpart the corresponding values are 0.65–0.66 *e*. Although the Mulliken analysis does not give a realistic insight into the charge distribution, this tells us that the Pb atoms have a much larger overlap with the iodide ions than with the bromide ions, which affects the binding energy of the Pb 4f levels.

An approximate estimation of the perovskite stoichiometry can be made using the relative intensities of the experimental

core levels. In such a calculation one needs to take into account the differential cross sections including asymmetry parameters and the angle between the photoelectrons and the polarization direction of the X-rays.⁴⁰ In the present article we use atomic subshell photoionization cross sections and asymmetry parameters calculated by Trzhaskovskaya et al.,^{41,42} and the experimental angle was 0°. The stoichiometry estimation gives a I/Pb ratio of 3.4 ± 0.2 and a Br/Pb ratio of 2.5 ± 0.2 compared to the expected value 3. Comparing the lead and nitrogen, the N/Pb ratio is 0.8 ± 0.1 for CH₃NH₃PbI₃ and 0.6 ± 0.1 for CH₃NH₃PbBr₃ where the stoichiometric value is 1. The given error bars are results of a comparison when using different core levels for the respective element. For both perovskites the estimated stoichiometries indicate a lower amount of CH₃NH₃⁺ compared to lead halide ions. This could be related to the presence of metallic lead and a loss of halide atoms, which will be discussed further below.

In an earlier publication we discussed that the contribution from metallic lead could be due to losses of iodine atoms.¹⁴ To theoretically study this further, DFT calculations have been performed on undercoordinated CH₃NH₃PbI₃. We have simulated two different structures where two I atoms surrounding an octahedral Pb atom have been removed to generate vacancy structure 1 (where two cis I atoms are removed) and structure 2 (where two trans I atoms are removed) as in Figures 4a and 4b, respectively. In an undistorted structure, Pb–I axial bonds are 3.0–3.1 Å long whereas the equatorial (along the *c*-axis) Pb–I bond lengths are 3.3–3.4 Å. However, the bond lengths in the defect structures are significantly altered and the four Pb–I bond lengths around the undercoordinated Pb are 3.06, 3.21, 3.46, and 3.56 Å for the cis-defect and 3.06, 3.07, 3.62, and 3.65 Å for the trans-defect.

For the defect structures, we again used the $Z + 1$ approximation in the DFT framework to calculate the relative binding energy of the undercoordinated Pb atoms. In the calculations, undercoordinated Pb atoms for both defect structures are offset by −1 eV relative to the remaining Pb ions, which are aligned within 0.1 eV. In comparison to the experimental spectrum, the smaller peak, which is assigned to atomic Pb, is nearly 1.6 eV apart from the main peak. The larger chemical shift seen in the experimental spectrum in Figure 3 indicates that the created defects shown in Figure 4 do not describe a defect with a subset of Pb atoms in a sufficiently different environment to account for the experimental observation. A Mulliken charge analysis was attempted for the different Pb atoms in the electronic ground state of the

defect structure, but although there is a clear distinction between the Pb atoms in octahedral coordination and the defects, the magnitude of the charge difference corresponds to only 0.1 e . This is much smaller than the difference between the two materials and indicates that a charge analysis is not a suitable tool for discussing the core-level shifts.

The discussion above supports the conclusion that the observed features arise from undercoordinated Pb atoms grouped together forming larger clusters of metallic lead. Interestingly, a very recent report by Shkrob et al. based on electron paramagnetic resonance (EPR) measurements demonstrates the formation of lead clusters due to trapping of electrons by Pb^{2+} cations in several organolead halide perovskites.⁴³

Valence Levels. Above, the shifts in the Pb 4f core levels were discussed in terms of the differences in overlap between lead and the bromide and iodide ions. The latter, having a more extended and polarizable electron cloud, give an enhanced screening of the core hole. Similarly, variations of the valence levels could also be expected. The higher V_{oc} observed for this perovskite¹² also indicates a changed position of the valence band or conduction band edge.

The experimental valence levels are shown in the top part of Figure 5. The thin red lines indicate where the linearly

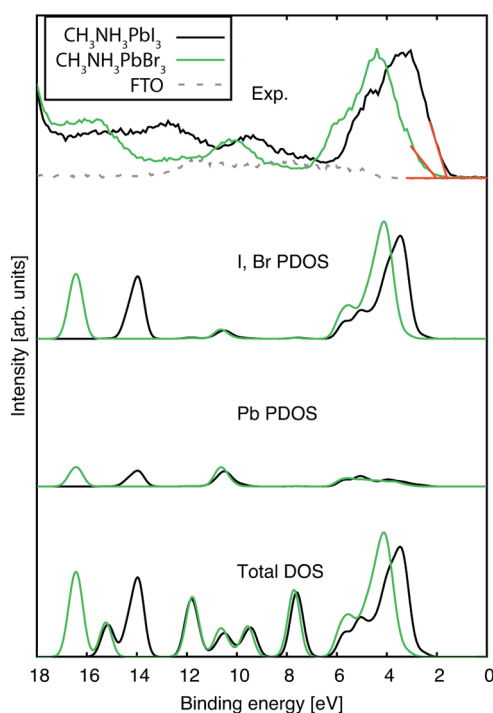


Figure 5. Experimental valence spectra compared to calculated total and partial DOS. The measured valence spectra of clean FTO is scaled in intensity using the Sn 4d level from the FTO/ $\text{CH}_3\text{NH}_3\text{PbI}_3$ sample to indicate the maximum FTO contribution to the valence levels of the FTO/perovskite samples. The thin red lines indicate where the linearly extrapolated experimental spectra intersects with the baseline.

extrapolated experimental spectra intersects with the baseline, which is used to estimate the energy of the valence band edge. The intersects are observed at binding energies of 1.55 and 2.05 eV. Based on this treatment, it can be seen that the valence band edge is approximately at a 0.5 eV higher binding energy for the $\text{CH}_3\text{NH}_3\text{PbBr}_3$ perovskite compared to $\text{CH}_3\text{NH}_3\text{PbI}_3$, similar to the findings in earlier work.¹⁸ In addition to the shift

of the main feature at the valence-band edge around 2–7 eV, we can also observe shifts at the peak at 9–10 eV and in the feature at 12–16 eV. Since the FTO substrate is slightly visible through the perovskite film, the substrate contributes to the perovskite valence spectra with some extra background in the region 4–14 eV. FTO is however slightly more visible in the FTO/ $\text{CH}_3\text{NH}_3\text{PbI}_3$ sample, and the dotted gray line in Figure 5 indicates the contribution from the FTO to the valence levels in this sample.

The calculated total DOS and the Br, I, and Pb PDOS are also included in Figure 5. It is clearly evident that the experimentally observed shift of the valence band is in qualitative agreement with the calculated DOS, where also a shift can be seen. The alignment of the calculated PDOS from the two materials is based on the procedure using a merged structure as described in the Computational Details. The broadening applied to the calculated DOS gives theoretical spectra with a shape that is, for both perovskites, comparable to the experimentally measured spectra. Despite the similar shape, there is a small difference in binding energy shift of the obtained intensity maxima of the outermost valence levels (3–5 eV) when comparing experiment with theory. In the theoretical spectra, this binding energy shift is 0.6 eV whereas in the experimental spectra it is 1 eV, with the $\text{CH}_3\text{NH}_3\text{PbBr}_3$ perovskite having a higher binding energy.

Neglecting the electronic states of the CH_3NH_3^+ cations, and considering only the lead halide contribution to the photoelectron spectrum, the I, Br, and Pb PDOS can be used to analyze the experimental spectra. The similarity with the combined Pb and I PDOS spectra and the experimental results suggest that the lack of nitrogen and carbon signal in the binding energy region shown in Figure 5 comes from a low photoionization cross section of such light elements at high photon energies. The agreement of the experimental and simulated valence spectra also holds for the structure above the valence band edge, at binding energies between 6 and 18 eV. From the partial DOS it is seen that, for the $\text{CH}_3\text{NH}_3\text{PbBr}_3$ perovskite, both the halide and lead PDOS are shifted toward higher binding energy (at the binding energies 10.5 and 14–17 eV). The shift of the Pb PDOS in this region agrees with the core-level shifts of Pb, but the magnitude of the shift is larger (in particular for the feature shifting from 14 eV for $\text{CH}_3\text{NH}_3\text{PbI}_3$ to 17 eV for $\text{CH}_3\text{NH}_3\text{PbBr}_3$). Thus, both the experimental data and the calculations give further evidence that it is the halide atoms that to a large extent determines the binding energy position of the valence lead levels.

To gain more insight into the orbitals involved in the bonding, we present the total DOS and PDOS of the two perovskites in Figure 6, where the atomic PDOS is further partitioned into their orbital contributions. From the figure it can be clearly inferred that, at the valence band edge, the contribution to the bonding comes from halide and lead p orbitals. Similarly, in the binding energy range 4–10 eV, the s and p orbitals from the halides and Pb contribute to the valence spectra. The higher energy range (above 10 eV) in the valence spectra primarily comes from s orbitals of the halides.

Since the two studied compounds have different detailed geometrical configurations, we wanted to get some insight into whether the difference seen in valence electronic structure is dependent on the geometrical configuration or the presence of different halides. In Figure 7 we therefore present the total DOS spectra for both the pristine perovskites along with their counterparts where I is replaced by Br in the crystal structure of

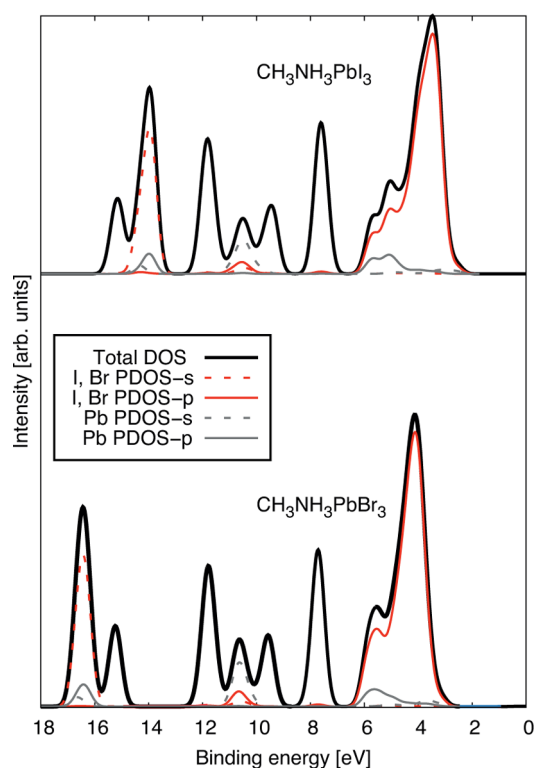


Figure 6. Calculated total and partial DOS for both perovskites.

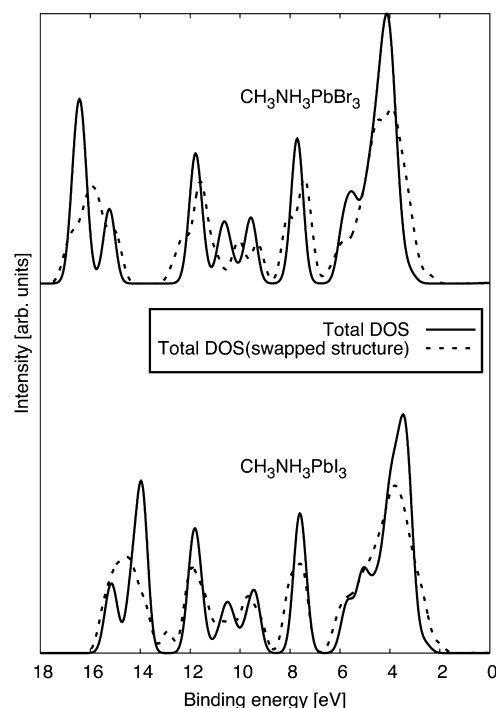


Figure 7. Total DOS of $\text{CH}_3\text{NH}_3\text{PbI}_3$ and $\text{CH}_3\text{NH}_3\text{PbBr}_3$ perovskites (solid lines) compared with corresponding TDOS from swapping the structure while keeping the halide moieties fixed (dotted lines).

the $\text{CH}_3\text{NH}_3\text{PbI}_3$ perovskite and vice versa. This figure depicts that the difference in calculated total DOS largely arises from the atomic contribution (I, Br) and less from the structures of the two perovskites. While electronegativity qualitatively explains the effect, electron affinity gives a more quantitative insight into the binding energy shifts. The experimental

electron affinity for gas phase Br (3.36 eV)^{44,45} and I (3.06 eV)^{45,46} atoms are shifted 0.3 eV relative each other. This only partially accounts for the shift in the valence band edge for the two perovskite compounds and differences in chemical bonding also have a substantial influence. As in the case of the Pb 4f core-level shifts, we assign the larger shift in the valence band edge in the perovskite compounds relative to the gas phase halides, to the difference in screening. The above discussion leads us to the conclusion that it is the inherent contributions coming largely from the halide ions, rather than the geometrical variations, which is manifested in the shift in the valence levels of the two perovskites.

The analysis above indicates that the binding energy of the valence band edge is thus dependent in a dual manner on the halide in the perovskite material. On the one hand, there is an intrinsic binding energy difference between Br 4p and I 5p as seen as a 0.3 eV difference in the I^- and Br^- ions in gas phase^{44,46} with a higher binding energy for ionization of Br^- . On the other hand, there are differences in overlap with neighboring lead ions which influence the valence electronic structure and is a consequence of differences in the chemical bonding.

Returning to the functional properties of the perovskites studied here, the differences in the binding energy of the valence band edges will affect the energy level alignment at interfaces with other materials in e.g. a solar cell. This will, together with the different band gaps, affect the performance of the device. A thorough determination of the band edge for a crystalline material would require some insight into the specific band dispersion linked to the frontier energy levels. A simple approach is to extrapolate the experimental data as shown in Figure 5. The experimental values taken from the extrapolations in Figure 5 can, together with optical bandgaps (1.55 and 2.3 eV for $\text{CH}_3\text{NH}_3\text{PbI}_3$ and $\text{CH}_3\text{NH}_3\text{PbBr}_3$, respectively^{47,48}), be used to draw the schematic energy level diagram in Figure 8.

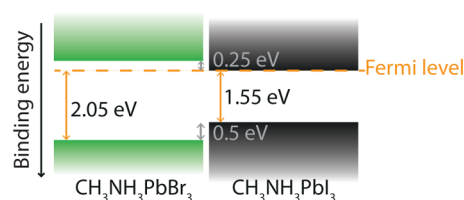


Figure 8. Schematic representation of the energy level diagrams for the two perovskites indicating the energy differences between the valence band edges and the Fermi level. Reported values of the optical bandgaps for the perovskites^{47,48} are used.

According to this figure, it is largely the valence band edge that differs when comparing the two perovskites, while the conduction band energies appear more similar (with a difference of 0.25 eV) very close to the Fermi level. Since the measurements are binding energy calibrated using the contribution from metallic lead, the work function of lead can be used to relate the Fermi level to the vacuum level. Reported work functions for lead varies between 4.0 and 4.25 eV,^{49–51} and thus, the energy difference between the conduction band edge and the vacuum level is also within this range for $\text{CH}_3\text{NH}_3\text{PbI}_3$ and 0.25 eV smaller for $\text{CH}_3\text{NH}_3\text{PbBr}_3$.

In this context, it is important to note that the energy level diagram of a solar cell device is dependent on the interfaces between the materials in the device. If a typical TiO_2 /perovskite/hole conductor solar cell device is regarded as a p–

i–n junction (where p stands for p-doped, i for intrinsic, and n for n-doped), the energy levels versus the Fermi level of the intrinsic perovskite varies between the n-doped TiO_2 and the p-doped hole conductor (similarly to band bending). Such variations were recently demonstrated with HAXPES when comparing a thick $\text{CH}_3\text{NH}_3\text{PbI}_{3-x}\text{Cl}_x$ film with $\text{TiO}_2/\text{CH}_3\text{NH}_3\text{PbI}_{3-x}\text{Cl}_x$ and $\text{Al}_2\text{O}_3/\text{CH}_3\text{NH}_3\text{PbI}_{3-x}\text{Cl}_x$ interfaces.³² In interfacial measurements, the observed energy level alignment at the TiO_2 /perovskite and perovskite/hole conductor interfaces can be dependent on the probe depth of the experiment versus perovskite thickness. In this study, the thickness is similar for the $\text{CH}_3\text{NH}_3\text{PbI}_3$ and the $\text{CH}_3\text{NH}_3\text{PbBr}_3$ perovskites, and from the presence of the substrate FTO signal, the layer thickness is estimated to be below 10 nm on average. Moreover, the Fermi level in both materials is aligned with the metallic lead, expected to have very similar work functions in both systems.

CONCLUSIONS

Electronic structures of two organolead halide perovskites ($\text{CH}_3\text{NH}_3\text{PbI}_3$ and $\text{CH}_3\text{NH}_3\text{PbBr}_3$) are addressed using photoelectron spectroscopy measurements. DFT-based modeling of the structures of these two perovskites and computation of DOS spectra successfully led us to rationalize the correct trends in corresponding experimental valence level spectra. Both measurements and computations show a shift of the valence band edges where there is a higher binding energy of the edge for the $\text{CH}_3\text{NH}_3\text{PbBr}_3$ perovskite. In our key findings, we assert that it is the nature of the halide ion rather than the geometrical configuration of the perovskites, which causes this shift, due to an intrinsic binding energy difference and to difference in overlap and thus in chemical bonding. The detailed electronic structure of the halide atom therefore has a major impact when designing effective solar cells, which are based on energy matching at several interfaces, and this in turn decides their performance. We have also attempted to model the appearance of metallic lead, which has recently been related to a charge trapping process⁴³ and playing a decisive role in the photovoltaic efficiency. The present findings might be pertinent in fine-tuning the performance of the solar cells.

AUTHOR INFORMATION

Corresponding Authors

*E-mail rebecka.lindblad@physics.uu.se (R.L.).

*E-mail hakan.rensmo@physics.uu.se (H.R.).

Notes

The authors declare no competing financial interest.

ACKNOWLEDGMENTS

This work was supported by the Swedish Energy Agency (STEM P34131-1), the Göran Gustafsson Foundation, the Carl Trygger Foundation, StandUp for Energy, the Swedish Research Council (2012-4721 and 2012-2419), and the European Community's Seventh Framework Programme (FP/2007-2013 under Grant Agreement 226716). We acknowledge the Helmholtz-Zentrum Berlin, BESSY II, for provision of synchrotron radiation at beamline KMC-1 and thank Mihaela Gorgoi for assistance. The theoretical modelling was made possible through generous allocations of computer time provided by the Swedish National Infrastructure for Computing (SNIC) at the Swedish National Supercomputer Center (NSC) and the High Performance Computer Center North (HPC2N)

and Chalmers Centre for Computational Science and Engineering (C3SE), Sweden.

REFERENCES

- (1) Boix, P. P.; Nonomura, K.; Mathews, N.; Mhaisalkar, S. G. Current Progress and Future Perspectives for Organic/Inorganic Perovskite Solar Cells. *Mater. Today* **2014**, *17*, 16–23.
- (2) Snaith, H. J. Perovskites: The Emergence of a New Era for Low-Cost, High-Efficiency Solar Cells. *J. Phys. Chem. Lett.* **2013**, *4*, 3623–3630.
- (3) Grätzel, C.; Zakeeruddin, S. M. Recent Trends in Mesoscopic Solar Cells Based on Molecular and Nanopigment Light Harvesters. *Mater. Today* **2013**, *16*, 11–18.
- (4) Kojima, A.; Teshima, K.; Shirai, Y.; Miyasaka, T. Organometal Halide Perovskites as Visible-Light Sensitizers for Photovoltaic Cells. *J. Am. Chem. Soc.* **2009**, *131*, 6050–6051.
- (5) Kim, H.-S.; Lee, C.-R.; Im, J.-H.; Lee, K.-B.; Moehl, T.; Marchioro, A.; Moon, S.-J.; Humphry-Baker, R.; Yum, J.-H.; Moser, J. E.; et al. Lead Iodide Perovskite Sensitized All-Solid-State Submicron Thin Film Mesoscopic Solar Cell with Efficiency Exceeding 9%. *Sci. Rep.* **2012**, *2*, 591.
- (6) Burschka, J.; Pellet, N.; Moon, S.-J.; Humphry-Baker, R.; Gao, P.; Nazeeuruddin, M. K.; Graetzel, M. Sequential Deposition as a Route to High-Performance Perovskite-Sensitized Solar Cells. *Nature* **2013**, *499*, 316–319.
- (7) Lee, M. M.; Teuscher, J.; Miyasaka, T.; Murakami, T. N.; Snaith, H. J. Efficient Hybrid Solar Cells Based on Meso-Superstructured Organometal Halide Perovskites. *Science* **2012**, *338*, 643–647.
- (8) Conings, B.; Baeten, L.; De Dobbelaere, C.; D'Haen, J.; Manca, J.; Boyen, H.-G. Perovskite-Based Hybrid Solar Cells Exceeding 10% Efficiency with High Reproducibility Using a Thin Film Sandwich Approach. *Adv. Mater.* **2014**, *26*, 2041–2046.
- (9) Liu, M.; Johnston, M. B.; Snaith, H. J. Efficient Planar Heterojunction Perovskite Solar Cells by Vapour Deposition. *Nature* **2013**, *501*, 395–398.
- (10) Chen, Q.; Zhou, H.; Hong, Z.; Luo, S.; Duan, H.-S.; Wang, H.-H.; Liu, Y.; Li, G.; Yang, Y. Planar Heterojunction Perovskite Solar Cells via Vapor-Assisted Solution Process. *J. Am. Chem. Soc.* **2014**, *136*, 622–625.
- (11) Sun, S.; Salim, T.; Mathews, N.; Duchamp, M.; Boothroyd, C.; Xing, G.; Sum, T. C.; Lam, Y. M. The Origin of High Efficiency in Low-Temperature Solution-Processable Bilayer Organometal Halide Hybrid Solar Cells. *Energy Environ. Sci.* **2014**, *7*, 399–407.
- (12) Cai, B.; Xing, Y.; Yang, Z.; Zhang, W.-H.; Qiu, J. High Performance Hybrid Solar Cells Sensitized by Organolead Halide Perovskites. *Energy Environ. Sci.* **2013**, *6*, 1480–1485.
- (13) Schmidt, L. C.; Pertegás, A.; González-Carrero, S.; Malinkiewicz, O.; Agouram, S.; Mínguez Espallargas, G.; Bolink, H. J.; Galian, R. E.; Pérez-Prieto, J. Nontemplate Synthesis of $\text{CH}_3\text{NH}_3\text{PbBr}_3$ Perovskite Nanoparticles. *J. Am. Chem. Soc.* **2014**, *136*, 850–853.
- (14) Lindblad, R.; Bi, D.; Park, B.-w.; Oscarsson, J.; Gorgoi, M.; Siegbahn, H.; Odelius, M.; Johansson, E. M. J.; Rensmo, H. Electronic Structure of $\text{TiO}_2/\text{CH}_3\text{NH}_3\text{PbI}_3$ Perovskite Solar Cell Interfaces. *J. Phys. Chem. Lett.* **2014**, *5*, 648–653.
- (15) Wang, Y.; Gould, T.; Dobson, J. F.; Zhang, H.; Yang, H.; Yao, X.; Zhao, H. Density Functional Theory Analysis of Structural and Electronic Properties of Orthorhombic Perovskite $\text{CH}_3\text{NH}_3\text{PbI}_3$. *Phys. Chem. Chem. Phys.* **2014**, *16*, 1424–1429.
- (16) Even, J.; Pedesseau, L.; Jancu, J.-M.; Katan, C. Importance of Spin-Orbit Coupling in Hybrid Organic/Inorganic Perovskites for Photovoltaic Applications. *J. Phys. Chem. Lett.* **2013**, *4*, 2999–3005.
- (17) Mosconi, E.; Amat, A.; Nazeeruddin, M. K.; Grätzel, M.; De Angelis, F. First-Principles Modeling of Mixed Halide Organometal Perovskites for Photovoltaic Applications. *J. Phys. Chem. C* **2013**, *117*, 13902–13913.
- (18) Schulz, P.; Edri, E.; Kirmayer, S.; Hodes, G.; Cahen, D.; Kahn, A. Interface Energetics in Organo-Metal Halide Perovskite-Based Photovoltaic Cells. *Energy Environ. Sci.* **2014**, *7*, 1377–1381.

- (19) Bi, D.; Yang, L.; Boschloo, G.; Hagfeldt, A.; Johansson, E. M. J. Effect of Different Hole Transport Materials on Recombination in $\text{CH}_3\text{NH}_3\text{PbI}_3$ Perovskite-Sensitized Mesoscopic Solar Cells. *J. Phys. Chem. Lett.* **2013**, *4*, 1532–1536.
- (20) Gorgoi, M.; Svensson, S.; Schäfers, F.; Öhrwall, G.; Mertin, M.; Bressler, P.; Karis, O.; Siegbahn, H.; Sandell, A.; Rensmo, H.; et al. The High Kinetic Energy Photoelectron Spectroscopy Facility at BESSY Progress and First Results. *Nucl. Instrum. Methods Phys. Res., Sect. A* **2009**, *601*, 48–53.
- (21) Hinnen, C.; van Huong, C. N.; Marcus, P. A Comparative X-ray Photoemission Study of $\text{Bi}_2\text{Sr}_2\text{CaCu}_2\text{O}_8^+$ and $\text{Bi}_{1.6}\text{Pb}_{0.4}\text{Sr}_2\text{CaCu}_2\text{O}_8^+$. *J. Electron Spectrosc. Relat. Phenom.* **1995**, *73*, 293–304.
- (22) Stoumpos, C. C.; Malliakas, C. D.; Kanatzidis, M. G. Semiconducting Tin and Lead Iodide Perovskites with Organic Cations: Phase Transitions, High Mobilities, and Near-Infrared Photoluminescent Properties. *Inorg. Chem.* **2013**, *52*, 9019–9038.
- (23) Poglitsch, A.; Weber, D. Dynamic Disorder in Methylammoniumtrihalogenoplumbates(II) Observed by Millimeter-Wave Spectroscopy. *J. Chem. Phys.* **1987**, *87*, 6373–6378.
- (24) CPMD. Copyright IBM Corporation 1990–2012; MPI für Festkörperforschung: Stuttgart, Germany, 1997–2001; www.cpmid.org.
- (25) CP2K version 2.3. The CP2K developers group, 2012; http://www.cp2k.org/.
- (26) Becke, A. D. Density-Functional Exchange-Energy Approximation with Correct Asymptotic Behavior. *Phys. Rev. A* **1988**, *38*, 3098–3100.
- (27) Lee, C.; Yang, W.; Parr, R. G. Development of the Colle-Salvetti Correlation-Energy Formula into a Functional of the Electron Density. *Phys. Rev. B* **1988**, *37*, 785–789.
- (28) Grimme, S. Semiempirical GGA-Type Density Functional Constructed with a Long-Range Dispersion Correction. *J. Comput. Chem.* **2006**, *27*, 1787–1799.
- (29) Troullier, N.; Martins, J. L. Efficient Pseudopotentials for Plane-Wave Calculations. *Phys. Rev. B* **1991**, *43*, 1993–2006.
- (30) Kleinman, L.; Bylander, D. M. Efficacious Form for Model Pseudopotentials. *Phys. Rev. Lett.* **1982**, *48*, 1425–1428.
- (31) Goedecker, S.; Teter, M.; Hutter, J. Separable Dual-Space Gaussian Pseudopotentials. *Phys. Rev. B* **1996**, *54*, 1703–1710.
- (32) Hartwigsen, C.; Goedecker, S.; Hutter, J. Relativistic Separable Dual-Space Gaussian Pseudopotentials from H to Rn. *Phys. Rev. B* **1998**, *58*, 3641–3662.
- (33) VandeVondele, J.; Krack, M.; Mohamed, F.; Parrinello, M.; Chassaing, T.; Hutter, J. Quickstep: Fast and Accurate Density Functional Calculations Using a Mixed Gaussian and Plane Waves Approach. *Comput. Phys. Commun.* **2005**, *167*, 103–128.
- (34) VandeVondele, J.; Hutter, J. An Efficient Orbital Transformation Method for Electronic Structure Calculations. *J. Chem. Phys.* **2003**, *118*, 4365–4369.
- (35) Krack, M. Pseudopotentials for H to Kr Optimized for Gradient-Corrected Exchange-Correlation Functionals. *Theor. Chem. Acc.* **2005**, *114*, 145–152.
- (36) VandeVondele, J.; Hutter, J. Gaussian Basis Sets for Accurate Calculations on Molecular Systems in Gas and Condensed Phases. *J. Chem. Phys.* **2007**, *127*, 114105.
- (37) Campbell, J.; Papp, T. Widths of the Atomic K-N7 Levels. *At. Data Nucl. Data Tables* **2001**, *77*, 1–56.
- (38) Atuchin, V.; Isaenko, L.; Kesler, V.; Tarasova, A. Single Crystal Growth and Surface Chemical Stability of $\{\text{KPb}_2\text{Br}_5\}$. *J. Cryst. Growth* **2011**, *318*, 1000–1004.
- (39) Tarasova, A.; Isaenko, L.; Kesler, V.; Pashkov, V.; Yeliseyev, A.; Denysyuk, N.; Khyzhun, O. Electronic Structure and Fundamental Absorption Edges of KPb_2Br_5 , $\text{K}_{0.5}\text{Rb}_{0.5}\text{Pb}_2\text{Br}_5$, and RbPb_2Br_5 Single Crystals. *J. Phys. Chem. Solids* **2012**, *73*, 674–682.
- (40) Yeh, J.; Lindau, I. Atomic Subshell Photoionization Cross Sections and Asymmetry Parameters: 1 Z 103. *Atom. Data Nucl. Data* **1985**, *32*, 1–155.
- (41) Trzhaskovskaya, M.; Nefedov, V.; Yarzhevsky, V. Photoelectron Angular Distribution Parameters for Elements Z=1 to Z=54 in the Photoelectron Energy Range 100–5000 eV. *Atom. Data Nucl. Data* **2001**, *77*, 97–159.
- (42) Trzhaskovskaya, M.; Nefedov, V.; Yarzhevsky, V. Photoelectron Angular Distribution Parameters for Elements Z=55 to Z=100 in the Photoelectron Energy Range 100–5000 eV. *Atom. Data Nucl. Data* **2002**, *82*, 257–311.
- (43) Shkrob, I. A.; Marin, T. W. Charge Trapping in Photovoltaically Active Perovskites and Related Halogenoplumbate Compounds. *J. Phys. Chem. Lett.* **2014**, *5*, 1066–1071.
- (44) Blondel, C.; Cacciani, P.; Delsart, C.; Trainham, R. High-Resolution Determination of the Electron Affinity of Fluorine and Bromine Using Crossed Ion and Laser Beams. *Phys. Rev. A* **1989**, *40*, 3698–3701.
- (45) Bartmess, J. In *NIST Chemistry WebBook, NIST Standard Reference Database Number 69*; Linstrom, P., Mallard, W., Eds.; National Institute of Standards and Technology: Gaithersburg, MD, http://webbook.nist.gov; retrieved March 27, 2014.
- (46) Pelaez, R. J.; Blondel, C.; Delsart, C.; Drag, C. Pulsed Photodetachment Microscopy and the Electron Affinity of Iodine. *J. Phys. B: At. Mol. Opt. Phys.* **2009**, *42*, 125001.
- (47) Grätzel, M. The Light and Shade of Perovskite Solar Cells. *Nat. Mater.* **2014**, *13*, 838–842.
- (48) Noh, J. H.; Im, S. H.; Heo, J. H.; Mandal, T. N.; Seok, S. I. Chemical Management for Colorful, Efficient, and Stable Inorganic-Organic Hybrid Nanostructured Solar Cells. *Nano Lett.* **2013**, *13*, 1764–1769.
- (49) Peredkov, S.; Sorensen, S. L.; Rosso, A.; Öhrwall, G.; Lundwall, M.; Rander, T.; Lindblad, A.; Bergersen, H.; Pokapanich, W.; Svensson, S.; Björneholm, O.; Mårtensson, N.; Tchapyguine, M. Size Determination of Free Metal Clusters by Core-Level Photoemission from Different Initial Charge States. *Phys. Rev. B* **2007**, *76*, 081402.
- (50) Bahn, J.; OelSSner, P.; Köther, M.; Braun, C.; Senz, V.; Palutke, S.; Martins, M.; Rühl, E.; Ganteför, G.; Möller, T.; von Issendorff, B.; Bauer, D.; Tiggesbäumker, J.; Meiwes-Broer, K.-H. Pb 4f Photoelectron Spectroscopy on Mass-Selected Anionic Lead Clusters at FLASH. *New J. Phys.* **2012**, *14*, 075008.
- (51) Michaelson, H. B. The Work Function of the Elements and Its Periodicity. *J. Appl. Phys.* **1977**, *48*, 4729–4733.
- (52) Leijtens, T.; Stranks, S. D.; Eperon, G. E.; Lindblad, R.; Johansson, E. M. J.; McPherson, I. J.; Rensmo, H.; Ball, J. M.; Lee, M. M.; Snaith, H. J. Electronic Properties of Meso-Superstructured and Planar Organometal Halide Perovskite Films: Charge Trapping, Photodoping, and Carrier Mobility. *ACS Nano* **2014**, *8*, 7147–7155.